

# Benchtop magnetic shielding for benchmarking atomic magnetometers

P. J. Hobson<sup>1,+</sup>, N. Holmes<sup>1,2</sup>, C. Morley<sup>1</sup>, A. Davis<sup>1</sup>, M. Packer<sup>1</sup>, T. X. Smith<sup>1</sup>, B. Styles<sup>3</sup>, P. Patel<sup>3</sup>, S. Raudonyte<sup>3</sup>, J. Chalmers<sup>3</sup>, D. Holmes<sup>3</sup>, R. Harrison<sup>3</sup>, D. Woolger<sup>3</sup>, D. Sims<sup>3</sup>, M. J. Brookes<sup>1,2</sup>, R. W. Bowtell<sup>1,2</sup>, and T. M. Fromhold<sup>1</sup>

<sup>1</sup>School of Physics and Astronomy, University of Nottingham, NG7 2RD, United Kingdom

<sup>2</sup>Sir Peter Mansfield Imaging Centre, University of Nottingham, NG7 2RD, United Kingdom

<sup>3</sup>Magnetic Shields Ltd, Staplehurst, TN12 0DS, United Kingdom

<sup>+</sup>[peter.hobson@nottingham.ac.uk](mailto:peter.hobson@nottingham.ac.uk)

**Abstract**—We present a benchtop magnetic shield in which ultra-sensitive quantum magnetometers may be developed and tested. We optimise the geometry of four mumetal cylinders to maximise shielding efficiency while maintaining Johnson noise  $< 15 \text{ fT}/\sqrt{\text{Hz}}$ . Experimental measurements at the shield's centre show axial shielding efficiency of  $(4.2 \pm 0.1) \times 10^5$  at 0.1 Hz. Nine flexible printed circuit boards are housed inside the shield to actively generate three uniform fields, which all deviate from perfect uniformity by  $\leq 0.5\%$  along 50% of the inner shield axis, and five linear field gradients and one second-order gradient, which all deviate by  $\leq 4\%$  from perfect linearity and curvature, respectively. Together, the target field amplitudes are adjusted to minimise the remnant static field along 40% of the inner shield axis, as mapped using an atomic magnetometer. The active null reduces the norm of the magnitudes of the three uniform fields and six gradients by factors of 19.5 and 19.8, respectively, thereby reducing the total field from 1.68 nT to 230 pT.

**Index Terms**—electromagnetic measurements, flexible printed circuits, Fourier transforms, magnetic shielding, magnetometers

## I. INTRODUCTION

An exceptionally low and controlled magnetic field is required to reduce noise in fundamental physics experiments [1], [2] and to benchmark ultra-sensitive quantum magnetometers, including those based on NV-centres [3] and atomic vapours [4]–[6]. In particular, zero-field Optically Pumped Magnetometers (OPMs) [7], [8] have diverse applications from functional neuroimaging [9], [10] to rapid diagnostics of electric batteries [11], [12], but require low static fields to reduce projection errors [13] and nonlinearities in sensor gain.

External magnetic fields may be attenuated by enclosing a region with passive shielding material. For low frequency shielding, high permeability materials, like *mumetal*, are used to divert magnetic flux. However, high permeability materials magnetise under applied fields, thereby limiting the shielding effect. Although this is mitigated by degaussing [14], some remnant magnetisation usually remains. Coil systems inside passive shields are used to null offsets induced by magnetisation and cancel leakage fields. These coils may be designed to account for the electromagnetic distortion induced by their coupling to passive shielding [15]–[19].

In this paper, we build, test, and operate a magnetic shield consisting of optimised nested mumetal cylinders and internal active coils. Firstly, we test the passive shielding of the mumetal cylinders. Then, we construct nine active coils, housed on nested flexible Printed Circuit Boards (flex-PCBs)

inside the inner mumetal shield, which are designed to null static offset fields. The coupling of the active and passive parts is included *a priori* in the design process to enhance the nulling process. We characterise the flex-PCBs in situ and use them to null the residual field along the inner shield axis, which is mapped by a zero-field OPM.

## II. PASSIVE SHIELDING

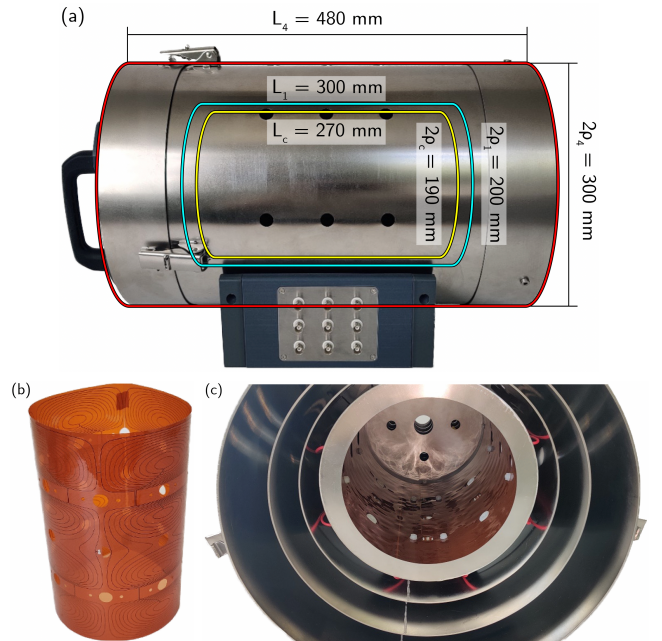


**Fig. 1:** The benchtop shield consists of four nested mumetal cylinders of outer radius  $\rho_4 = 150 \text{ mm}$  and length  $L_4 = 480 \text{ mm}$  [red] and inner radius  $\rho_1 = 100 \text{ mm}$  and length  $L_1 = 300 \text{ mm}$  [blue], which enclose a co-axial and co-centred set of rolled flex-PCBs of outer radius  $\rho_c = 95 \text{ mm}$  and length  $L_c = 270 \text{ mm}$  [yellow]. (a) Side view of the shield and end caps, (b) a rolled PCB, and (c) multiple PCBs housed inside the shield with the end cap removed.

The passive shielding is constructed from four benchtop-sized nested co-axial and co-centred mumetal cylinders with access holes (Fig. 1). The inner cylinder is of radius  $\rho_1 = 100 \text{ mm}$  and length  $L_1 = 300 \text{ mm}$  and is constructed from 0.5 mm thick mumetal to minimise the shield-induced Johnson noise [20]. The geometries of the exterior mumetal cylinders are selected using the NGS-II genetic algorithm [21] coupled to Finite Element Method simulations (COMSOL Mul-

tiphysics®) to maximise the shielding efficiency,  $SE_{A,T} = |\mathbf{B}^{\text{unshielded}}/\mathbf{B}^{\text{shielded}}|$ , along and transverse to the shield's axis ( $A/T$ ), following the method in Ref. 22.

$f$	$SE_A \times 10^5$
0.1	$4.2 \pm 0.1$
1	$5.5 \pm 0.1$
50	$> 10$

**TABLE I:** Axial shielding efficiency,  $SE_A$ , at the centre of the benchtop shield subject to a spatially-uniform oscillatory field of frequency,  $f$ , and peak-to-peak amplitude  $B_{0z} \sim 90 \mu\text{T}$ , as measured using a fluxgate magnetometer (Mag-13, Bartington Instruments).

We degauss the shield by driving sinusoidal current with a peak-to-peak amplitude of 4 A at a frequency of 8 Hz for 15 s through four loops, which are wrapped along the axis of the inner shield, and then ramping down the current linearly over 45 s. We then apply time-varying fields with amplitudes of  $\sim 45 \mu\text{T}$ , matching the strength of the geomagnetic field. These are generated using an external Helmholtz pair of radius 617 mm, which generates a field that deviates by  $< 1.5\%$  from perfect uniformity in free space along its axis between  $z = [-L_1/2, L_1/2]$ . We determine  $SE_{A,T}$  by calculating the Fast Fourier Transform (FFT) of the measured field at the shield's centre. The  $SE_A$  at the shield's centre is presented in Table I. As the applied frequency increases, eddy currents induced in the shield increase and enhance  $SE_A$  further. At 50 Hz, the axial field transmitted through the shield is less than the magnetometer noise floor, and so  $SE_A > 10^6$ . Similarly,  $SE_T > 10^6$  is measured at  $f = [0.1, 1, 50]$  Hz. However, even in the scenario where the shielding efficiency is lowest,  $SE_A = (4.2 \pm 0.1) \times 10^5$  at  $f = 0.1$  Hz, the axial field transmitted through the shield is much less than the measured static field offset,  $> 1$  nT, which results from remnant magnetisation of the mumetal after degaussing.

### III. FLEX-PCB COILS

Next, we consider how to null static offsets using active field coils. Using the theoretical model in Ref. 15, we design nine flex-PCBs to generate nine low-order magnetic field harmonics within the central half length and diameter of the inner shield cylinder. We choose to generate the full set of uniform fields and linear field gradients (see Table II), and a single quadratic field gradient with respect to axial position,  $d^2B_z/dz^2$ , to help offset the difference between  $SE_A$  and  $SE_T$ . The PCBs are co-centred and co-axial to the shield cylinder and extend over an outer radius  $\rho_c = 95$  mm and length  $L_c = 270$  mm.

The wire patterns which generate the  $dB_y/dx$  and  $B_z$  fields are presented in Fig. 2. These patterns are selected according to which best emulates the continuum current [15] but is manufacturable, i.e. the individual wires are greater than 0.8 mm apart and do not intersect with the access holes. The PCBs are made of polyimide of 0.26 mm depth into which copper tracks comprising the wire patterns are printed and are connected together in series across two flex-PCB layers with vias. The unwanted magnetic fields generated by the connecting tracks are reduced by including tracks on the second PCB layer with opposite current flow. The current

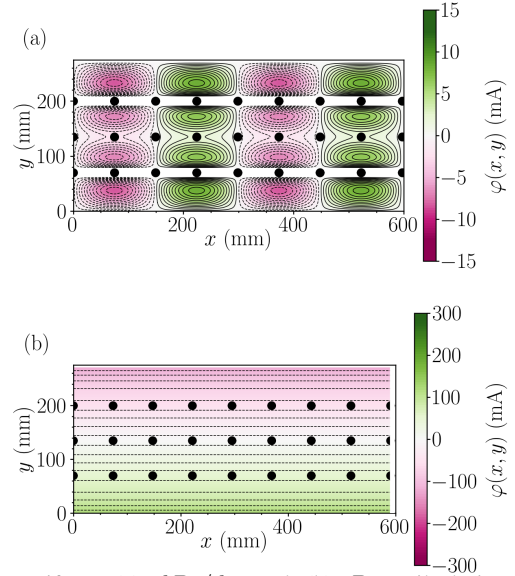


**Fig. 2:** Uniform (a)  $dB_y/dx$  and (b)  $B_z$  coil designs. Black solid and dashed linestyles show opposite current flow directions; green to white to pink colour shows the value of the current flow streamfunction,  $\psi$ , from positive to zero to negative [scale right]; and black circles show access holes. The uniform  $dB_y/dx$  coil is rolled along  $x$  to form a cylinder of radius 94.8 mm (Fig. 1b), whereas the uniform  $B_z$  coil is rolled into a cylinder of radius 92.9 mm. The coils have different radii to allow them to be nested inside each other.

pattern which generates the uniform  $B_z$  field is composed of current loops in series, which are constructed by soldering bridges across the PCB once it is rolled. The  $dB_y/dx$  current pattern does not require solder bridges as it does not cross the edge of the PCB. The uniform  $B_z$  PCB has a track width of 1.4 mm to allow 2 A of current to be passed to produce strong axial biasing ( $\sim 150 \mu\text{T}$ , without heating the shield above  $40^\circ\text{C}$  from  $20^\circ\text{C}$ ) whereas the remaining PCBs have track widths of 0.4 mm to allow 500 mA of current. The flex-PCBs are nested inside a nylon tube and have a radial thickness of 2.5 mm in situ, including solder bridges.

The magnetic fields generated by each flex-PCB are measured by driving sinusoidal current through each PCB sequentially at a frequency of 1 Hz for 10 s and taking the FFT of the measured field. We present the profiles generated by the  $B_y$ ,  $B_z$ ,  $dB_y/dx$ ,  $dB_y/dz$ ,  $dB_z/dz$ , and  $d^2B_z/dz^2$  PCBs in Fig. 3, evaluated along the shield's axis, except for the  $dB_y/dx$  PCB which is evaluated radially as it is designed to generate zero field along the shield's axis. The generated fields show close agreement to the target fields within the target region, and rapidly deviate outside of it, thus minimising the power consumption required to generate the desired field profile. We examine the deviation from perfect uniformity of the target fields generated by the uniform  $B_y$  and  $B_z$  PCBs in Fig. 4. The  $B_z$  profile deviates more than the  $B_y$  profile because of small error fields generated by the connections across the  $B_z$  PCB. Notwithstanding this, the fields generated by the uniform field-generating PCBs deviate from target only by  $\leq 0.5\%$  within the target region and compare favourably to other systems optimised in similar contexts [23]. The remaining PCBs are

$N$	Target field	Target field harmonic	Coil efficiency, $B_0/I$ (nT/(Amm $^{(N-1)}$ ))	$\max( \Delta(B/r^{(N-1)}) )$ (%)	Active nulling ratio, $ C $
1	$B_x$	$B_0\hat{x}$	$68.9 \pm 0.01$	$0.21 \pm 0.01$	11.3
	$B_y$	$B_0\hat{y}$	$68.7 \pm 0.01$	$0.22 \pm 0.01$	34.0
	$B_z$	$B_0\hat{z}$	$74.2 \pm 0.01$	$0.44 \pm 0.01$	13.1
2	$dB_x/dx$	$B_0(x\hat{x} - y\hat{y})$	$0.97 \pm 0.01$	$4 \pm 2$	—
	$dB_y/dx$	$B_0(y\hat{x} + x\hat{y})$	$0.94 \pm 0.01$	$4 \pm 2$	—
	$dB_x/dz$	$B_0(z\hat{x} + x\hat{z})$	$0.43 \pm 0.01$	$2 \pm 1$	62.4
	$dB_y/dz$	$B_0(z\hat{y} + y\hat{z})$	$0.44 \pm 0.01$	$2 \pm 1$	6.0
	$dB_z/dz$	$B_0(-x\hat{x} - y\hat{y} + 2z\hat{z})$	$1.10 \pm 0.01$	$1 \pm 1$	9.4
3	$d^2B_z/dz^2$	$B_0(-3xz\hat{x} - 3yz\hat{y} + 2z^2\hat{z})$	$0.018 \pm 0.001$	$4 \pm 2$	1.5

**TABLE II:** The benchtop shield contains nine nested flex-PCBs which generate three order  $N = 1$  uniform harmonics, five  $N = 2$  linear harmonics, and one  $N = 3$  quadratic harmonic, with specific variations along the Cartesian unit vectors,  $(\hat{x}, \hat{y}, \hat{z})$ . The mean field strength,  $B_0$ , per unit current,  $I$ , is calculated by averaging the measured field along  $\hat{z}$  between  $z = [0, L_1/4]$ , except for the  $dB_x/dx$  and  $dB_y/dx$  fields which are averaged along  $\hat{x}$  between  $x = [0, \rho_1/2]$ . Over the same spatial regions, we also evaluate the maximum deviation from the target field,  $\Delta(B/r^{(N-1)}) = B/r^{(N-1)} - B_0$ , as a percentage of  $B_0$ . The fitted target field magnitudes between  $z = [-64, 56]$  mm reduce by absolute ratios,  $|C|$ , after active nulling (see section IV;  $dB_x/dx$  and  $dB_y/dx$  ratios undetermined as the field is nulled along  $\hat{z}$ ).

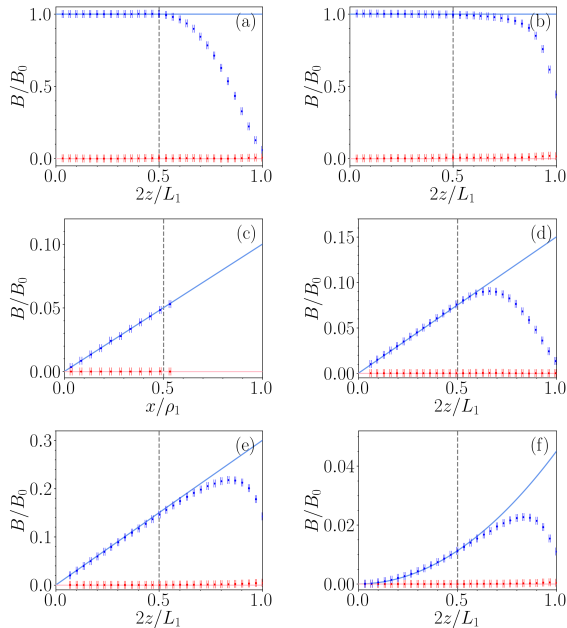


**Fig. 3:** Measured magnetic field (Mag-13, Bartington Instruments) in the target direction [blue] generated inside the benchtop shield of inner radius  $\rho_1 = 100$  mm and length  $L_1 = 300$  mm by the uniform (a)  $B_y$ , (b)  $B_z$ , (c)  $dB_y/dx$ , (d)  $dB_y/dz$ , (e)  $dB_z/dz$ , and (f)  $d^2B_z/dz^2$ , flex-PCB coils plotted along the  $z$ -axis except for (c) which is along the  $x$ -axis. The norm of the magnetic field in the other directions is measured [red] and is expected to be zero. Solid blue lines show perfect representations of the target fields and dashed grey lines show the edge of the target field region.

measured to generate fields which deviate from target by  $\leq 4\%$ ; we note that intrinsic deviations are likely to be even smaller as gradient field measurements are highly alignment-sensitive.

#### IV. ACTIVE NULLING

We follow the methodology in Ref. 24 to find each flex-PCB current required to null the remnant static field. We calculate the offsets of a tri-axial QZFM OPM (QuSpin Inc.) and then map the remnant field at 5 mm intervals along the  $z$ -axis by extracting the  $(B_x, B_y, B_z)$  values required to zero the field

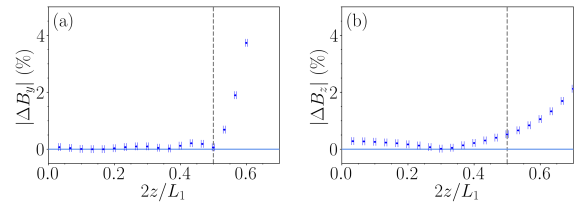


**Fig. 4:** Deviation between the measured and target fields for the uniform (a)  $B_y$  and (b)  $B_z$  flex-PCBs plotted versus position along the  $z$ -axis. Labelled as Fig. 3.

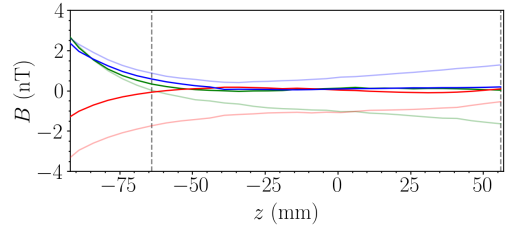


**Fig. 5:**  $B_x$ ,  $B_y$ , and  $B_z$  [green, red, and blue] measured using a tri-axial QZFM OPM (QuSpin Inc.) along the axis of the inner shield cylinder with [solid] and without [light] DC active background nulling between  $z = [-64, 56]$  mm [grey dashed lines].

using the onboard OPM coils. We then fit the measured fields between  $z = [-64, 56]$  mm to a spherical harmonic model, which assumes each coil generates the target field profile perfectly, before inverting to calculate the nulling currents. Finally, we re-measure the field along the  $z$ -axis with nulling currents applied (max.  $33 \mu\text{A}$ ), as shown in Fig. 5. Averaged over two runs, the active null reduces the mean magnetic field from 1.68 nT to 230 pT. Re-fitting the field to the harmonic model, we calculate that the norms of the magnitudes of the three target uniform fields and six target gradients are reduced by factors of 19.5 and 19.8 after nulling, respectively (see Table II). The remaining field is dominated by contributions from higher-order field harmonics at the edge of the null region. These may be reduced by using retrofitted additional coils, e.g. individually-driven simple building block coils [17].

In Fig. 6, we display the magnetic noise at the shield's centre measured over 5 minutes using the tri-axial OPM. Each

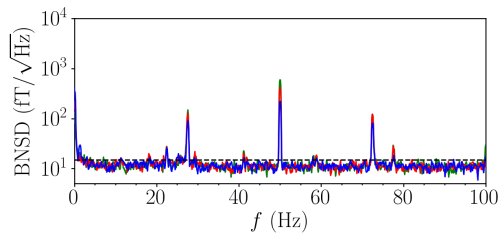


**Fig. 6:** Magnetic Noise Spectral Density (BNSD) [noise limit shown by black dashed line] measured by a tri-axial QZFM OPM (QuSpin Inc.) over 5 minutes under active nulling. Labelled as Fig. 5.

flex-PCB is driven in series with a 47 k $\Omega$  resistor so that the coil drivers do not add significant noise. Generally, the noise is limited by the magnetometer sensitivity, and so the shield-induced Johnson noise is  $< 15$  fT/ $\sqrt{\text{Hz}}$ . The noise floor peaks at  $\sim 750$  fT/ $\sqrt{\text{Hz}}$  at  $f = 50$  Hz due to mains electrical noise, with projections at  $f = [28, 72]$  Hz due to the OPM powerline.

## V. CONCLUSION

We have demonstrated a benchtop shield with low magnetic noise and optimised internal flex-PCBs, which improve the mean static shielding efficiency by a factor of 7.3 over 40% the inner shield length by nulling targeted harmonics in the residual field. Larger shields designed using the same methods could be used similarly to lightweight shielded rooms [25] for recording muscle [26] or gut activity [27]. Since these shields would require larger access holes, additional field-generating systems would be required to reduce leakage fields. Such coil systems may also supplement existing shielding, enabling its partial removal, e.g. for weight reduction in spacecraft [28].

## ACKNOWLEDGEMENTS

We acknowledge the support of the UK Quantum Technology Hub Sensors and Timing (EP/T001046/1).

## DECLARATIONS

P.J.H, M.P, D.S, M.J.B, R.W.B, and T.M.F have a worldwide patent (WO/2021/053356) which includes the coil design technique applied in this work. B.S, P.P, J.C, and D.W are employees of Magnetic Shields Limited (MSL), who sell benchtop shields commercially ([enq@magneticshields.co.uk](mailto:enq@magneticshields.co.uk)). S.J, D.H, and R.H are ex-employees of MSL. N.H, D.W, M.J.B, and R.W.B hold founding equity in Cerca Magnetics Limited, who commercialise OPM technology. C.M, A.D, and T.X.S declare no competing interests.

All supporting data may be made available on request.

## REFERENCES

- [1] J. Xu *et al.*, “The elimination of the effect of the external field in the Joule balance,” *IEEE Transactions on Instrumentation and Measurement*, vol. 69, no. 4, pp. 1745–1752, 2020.
- [2] S. Afach *et al.*, “Dynamic stabilization of the magnetic field surrounding the neutron electric dipole moment spectrometer at the Paul Scherrer Institute,” *Journal of Applied Physics*, vol. 116, 08 2014.
- [3] F. M. Stürmer *et al.*, “Integrated and portable magnetometer based on nitrogen-vacancy ensembles in diamond,” *Advanced Quantum Technologies*, vol. 4, no. 4, p. 2000111, 2021.
- [4] F. Bertrand *et al.*, “A 4 He vector zero-field optically pumped magnetometer operated in the Earth-field,” *Review of Scientific Instruments*, vol. 92, p. 105005, 10 2021.
- [5] S. P. Krzyzewski *et al.*, “Characterization of noise sources in a microfabricated single-beam zero-field optically-pumped magnetometer,” *Journal of Applied Physics*, vol. 126, no. 4, p. 044504, 2019.
- [6] P. Bevington *et al.*, “Non-destructive structural imaging of steelwork with atomic magnetometers,” *Applied Physics Letters*, vol. 113, no. 6, p. 063503, 2018.
- [7] I. Kominis *et al.*, “A subfemtotesla multichannel atomic magnetometer,” *Nature*, vol. 422, pp. 596–9, 05 2003.
- [8] V. K. Shah and R. T. Wakai, “A compact, high performance atomic magnetometer for biomedical applications,” *Physics in Medicine and Biology*, vol. 58, no. 22, pp. 8153–8161, 11 2013.
- [9] R. Hill *et al.*, “Using OPM-MEG in contrasting magnetic environments,” *NeuroImage*, vol. 253, p. 119084, 03 2022.
- [10] E. Boto *et al.*, “Triaxial detection of the neuromagnetic field using optically-pumped magnetometry: feasibility and application in children,” *NeuroImage*, vol. 252, p. 119027, 2022.
- [11] Y. Hu *et al.*, “Rapid online solid-state battery diagnostics with optically pumped magnetometers,” *Applied Sciences*, vol. 10, no. 21, 2020.
- [12] —, “Sensitive magnetometry reveals inhomogeneities in charge storage and weak transient internal currents in Li-ion cells,” *Proceedings of the National Academy of Sciences*, vol. 117, no. 20, pp. 10667–10672, 2020.
- [13] A. Borna *et al.*, “Cross-axis projection error in optically pumped magnetometers and its implication for magnetoencephalography systems,” *NeuroImage*, vol. 247, p. 118818, 2022.
- [14] Y. Fu *et al.*, “Suppression of nonuniform magnetic fields in magnetic shielding system for serf co-magnetometer,” *IEEE Transactions on Instrumentation and Measurement*, vol. 71, pp. 1–8, 2022.
- [15] M. Packer *et al.*, “Optimal inverse design of magnetic field profiles in a magnetically shielded cylinder,” *Physical Review Applied*, vol. 14, p. 054004, 11 2020.
- [16] —, “Planar coil optimization in a magnetically shielded cylinder,” *Physical Review Applied*, vol. 15, p. 064006, 6 2021.
- [17] —, “Magnetic field design in a cylindrical high-permeability shield: The combination of simple building blocks and a genetic algorithm,” *Journal of Applied Physics*, vol. 131, no. 9, p. 093902, 2022.
- [18] F. Zhao *et al.*, “Research on the design of axial uniform coils for residual field compensation in magnetically shielded cylinder,” *IEEE Transactions on Instrumentation and Measurement*, vol. 71, pp. 1–9, 2022.
- [19] H. Pang *et al.*, “Design of highly uniform field coils based on the magnetic field coupling model and improved PSO algorithm in atomic sensors,” *IEEE Transactions on Instrumentation and Measurement*, vol. 71, pp. 1–11, 2022.
- [20] S.-K. Lee and M. Romalis, “Calculation of magnetic field noise from high-permeability magnetic shields and conducting objects with simple geometry,” *Journal of Applied Physics*, vol. 103, pp. 084 904 – 084 904, 05 2008.
- [21] K. Deb *et al.*, “A fast and elitist multiobjective genetic algorithm: NSGA-II,” *IEEE Transactions on Evolutionary Computation*, vol. 6, no. 2, pp. 182–197, 2002.
- [22] P. J. Hobson *et al.*, “Optimised hybrid shielding and magnetic field control for emerging quantum technologies,” in *Quantum Technology: Driving Commercialisation of an Enabling Science II*, vol. 11881. SPIE, 2021, pp. 111 – 120.
- [23] —, “Bespoke magnetic field design for a magnetically shielded cold atom interferometer,” *Scientific Reports*, vol. 12, no. 1, jun 2022.
- [24] M. Rea *et al.*, “Precision magnetic field modelling and control for wearable magnetoencephalography,” *NeuroImage*, vol. 241, p. 118401, 07 2021.
- [25] N. Holmes *et al.*, “A lightweight magnetically shielded room with active shielding,” *Scientific Reports*, vol. 12, 08 2022.
- [26] P. J. Broser *et al.*, “Optically pumped magnetometers disclose magnetic field components of the muscular action potential,” *Journal of Electromyography and Kinesiology*, vol. 56, p. 102490, 2021.
- [27] C. Eichler *et al.*, “Effects of magnetogastrography sensor configurations in tracking slow wave propagation,” *Computers in Biology and Medicine*, vol. 129, p. 104169, 02 2021.
- [28] A. Junge and F. Marliani, “Prediction of DC magnetic fields for magnetic cleanliness on spacecraft,” in *2011 IEEE International Symposium on Electromagnetic Compatibility*, 2011, pp. 834–839.